Electronic Supplementary Material (ESI) for Journal of Materials Chemistry A.

Supporting Information

Inspired by Cu-driven conversion reaction: how anionic properties dictate the electrochemical performance of vanadium sulfide

Wenjuan Yang,[a] Kaihong Wang,[b] Wenbo Zhou,[a] Ningjing Luo,[a] Shuping Huang,[a] Yafeng Li,*[a] Kwun Nam Hui[b] and Mingdeng Wei*[a]

[a] *Fujian Key Laboratory of Electrochemical Energy Storage Materials, Fuzhou University, Fuzhou, Fujian 350116, China*
[b] Joint Key Laboratory of the Ministry of Education, Institute of Applied Physics and Materials Engineering, University of Macau, Avenida da Universidade, Taipa, Macau SAR 999078, China

*Corresponding author: Yafeng Li; Mingdeng Wei
E-mail address: liyf@fzu.edu.cn; wei-mingdeng@fzu.edu.cn

Experimental Section

Materials. Tetramethylthiuram disulfide (TMTD), vanadyl acetylacetonate (VO(acac)$_2$), tungsten hexachloride (WCl$_6$), sodium molybdate (Na$_2$MoO$_4$), thioacetamide (TAA) and copper (I) sulfide (Cu$_2$S) were purchased from Aladdin Reagent Co., Ltd. Na$_2$S, NaPF$_6$, NaCF$_3$SO$_3$, Cu(I)CF$_3$SO$_3$ salts, diglyme (DGM) and D$_2$O solvents were bought from Adamas Reagent, Ltd. Ethanol was from Sinopharm Chemical Reagent Co., Ltd. Electrolytes of 1.0 M NaPF$_6$/NaCF$_3$SO$_3$/NaFSI/NaTFSI/NaClO$_4$ diglyme were prepared by Suzhou Duoduo Chemical Technology Co., Ltd. All of the chemical reagents were used as received without further purification.

Synthetic methods

Synthesis of the VS$_2$/SNC composite

480 mg of TMTD was dissolved in 30 mL of DMF solvents and vigorously stirred evenly. Next, 265 mg of VO(acac)$_2$ was added into the above solution and stirred for 30 min. The homogeneous solution was transferred into a 50 mL teflon-lined stainless-steel autoclave and maintained at 180 °C for 24 h. The black precipitate (VS$_2$/SNC) was obtained after washing with ethanol for several times and dried in vacuum.

Synthesis of MoS$_2$

260 mg Na$_2$MoO$_4$ and 600 mg TAA were dissolved in the mixed solvent of 15 mL of DI water and 15 mL of ethanol DI water and stirred evenly. Subsequently, the above solution was transferred into a 50 mL teflon-lined stainless-steel autoclave and maintained at 200 °C for 24 h. The product of MoS$_2$ was obtained after washing with ethanol for several times and dried in vacuum.

Synthesis of WS$_2$

260 mg WCl$_6$ and 600 mg TAA were dissolved in 30 mL of DI water and stirred evenly, they were transferred into a 50 mL teflon-lined stainless-steel autoclave and maintained at 200 °C for 24 h subsequently. The product of WS$_2$ was obtained after washing with ethanol for several times and dried in vacuum.

Structural Characterization

X-ray diffraction (XRD) measurements were implemented using Rigaku Ultima IV with Cu Kα radiation. The elemental analyses were characterized by X-ray photoelectron spectroscopy (XPS, Thermo Scientific K-Alpha). The electrodes which disassembled from the batteries cycled for 200 times were etched 10 nm with argon plasma first, and then the XPS spectra were collected. The morphologies were investigated via scanning electron microscopy (SEM, Hitachi 4800) and Transmission electron microscopy (TEM, Thermo Scientific FEI). Raman spectra were captured using a microscope Raman spectrometer system (LabRAM HR, Horiba) with 532 nm laser excitations. Thermogravimetric analysis (TGA) was measured on a NETZSCH STA 449 C instrument using dried air as the working gas.

Electrochemical measurements

Electrochemical measurements were carried out using CR2025 coin-type cells. Specifically, the VS$_2$/SNC composite (or MoS$_2$, or WS$_2$ or Cu$_2$S), acetylene black and polyvinylidene fluoride (PVDF) were mixed with a mass ratio of 7: 2: 1, and the obtained slurry was pasted on the copper (Cu) or titanium (Ti) foil circular flakes. The final electrodes were dried at 80 °C for 12 h in a vacuum oven. Sodium slices were used as the counter and reference electrodes. The glass fibers (Whatman) were applied as the separators. The cells were assembled in a glovebox filled with highly pure argon gas (O$_2$ and H$_2$O levels < 1 ppm). Cyclic voltammetry (CV) was experimented on an electrochemical workstation (CHI 600C, shanghai, China). Electrochemical impedance spectroscopy (EIS) was carried out on an IVIUM Vertex electrochemical workstation. The batteries were cycled at 0.1 A g^{-1} for 10 times in advance, and then the in-situ EIS measurements were carried out at open circuit potential with 10 mV amplitude and in the frequency range from 10^{-1} to 10^5 Hz. Galvanostatic charge/discharge and galvanostatic intermittent titration (GITT) measurements were tested on an electrochemical workstation (Land CT 2001A, Wuhan, China) within a voltage range of 0.01 to 3.0 V (vs. Na$^+$/Na) at room temperature.

Characterization of electrolytes

The Na$_2$S$_8$ saturated solution was prepared by dissolving sulfur powder and Na$_2$S in DGM with a molar ratio of 7:1 inside an Ar-filled glove box at 25 °C, and 50 µL of the solution were separately pipetted into the two types of electrolytes with a volume of 5 mL and stirred evenly. Subsequently, the above two solutions were encapsulated in capillaries and their Raman spectra were captured. The XPS spectra were captured from the surfaces of Cu$_2$S and VS$_2$/SNC, which went through the electrolyte soaking treatments in advance, specifically, Cu$_2$S and VS$_2$/SNC were immersed in 1.0 M NaCF$_3$SO$_3$ (NaTf) DGM and hold in the sealed vessels for 5 days, then the vessels were opened to volatilized the DGM solvent at room temperature under Ar atmosphere, and then XPS measurements were performed

(The samples did not expose to the air during the whole process). Equal volume of DGM, 1.0 M NaTf DGM and 1.0 M $NaPF_6$ DGM solutions were separately added into equal volume of deteriorated water (D_2O), and the ^{1}H-NMR spectra of the electrolytes were collected by Bruker AV-II 400 MHz with D_2O was used as a reference. The retrieved electrolytes were obtained by rinsing the separators acquired from the corresponding batteries with 3 mL DGM for 48 h (the VS_2/SNC loading amount of the two batteries both were 0.42 mg cm^{-2}), and of which the UV-vis absorbance spectra were collected by using Shimadzu UV-2600 subsequently.

DFT Calculation Details

The cluster-based DFT calculations were performed in Gaussian (G09). [S1] The geometries and energies of the complexes used in this study were fully optimized without symmetry constraints at the B3LYP/def2-TZVP level of theory. [S2, S3] After the structure optimization, the binding energy (E_b) between two components was also calculated to illustrate the different interactions of $CF_3SO_3^-$ or PF_6^- with Na_2S_8, the binding energy was defined as following: $E_b=E_{total}-E_A-E_B$, where E_{total}, E_A, and E_B are the total energy of the A-B complexes, A part, and B part, respectively. Herein, A and B are referred to as $CF_3SO_3^-$, PF_6^- and Na_2S_8.

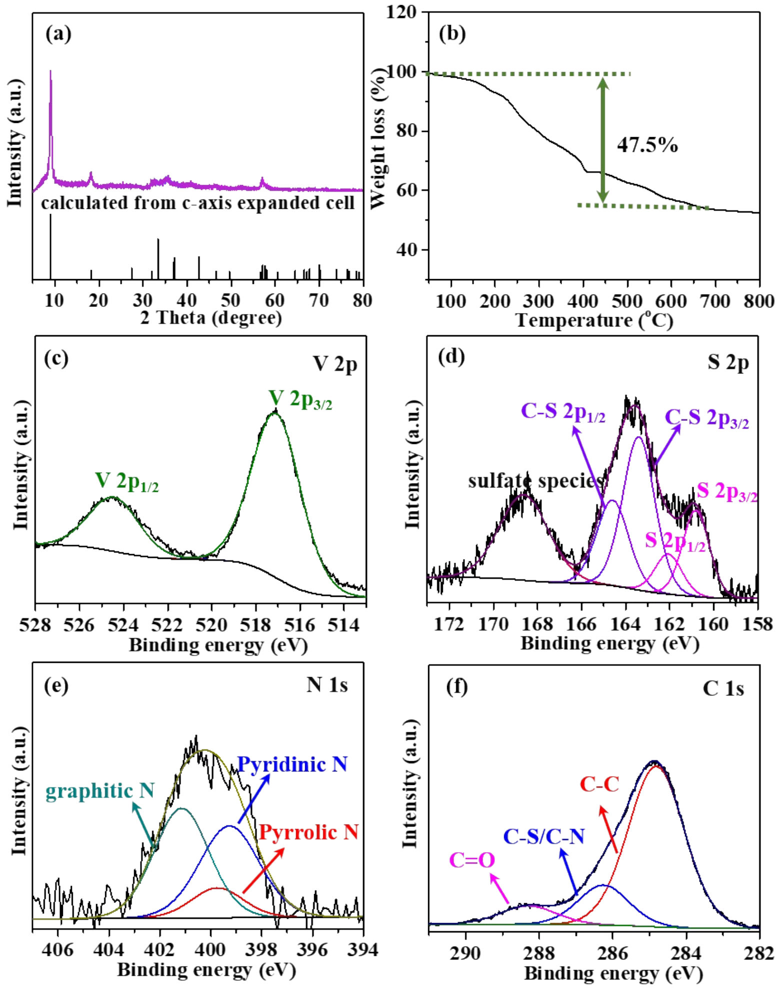

Fig. S1 (a) XRD pattern, (b) TGA curve recorded under an air atmosphere, and XPS spectra of (c) V 2p (d) S 2p (e) N 1s and (f) C 1s for the VS_2/SNC composite, respectively.

The X-ray diffraction (XRD) pattern of VS_2/SNC differentiates from the pristine VS_2 (JCPDS NO. 01-089-1640). [S4] In Fig. S1a, two peaks appear at 2 θ = 9.2° and 18.4° with a diploid relationship, which belong to the (001) and (002) crystal planes of VS_2, indicating a new lamellar structure with an enlarged interlayer spacing of 0.97 nm was formed. [S5] In Fig. S1b, the carbon content of the composite was calculated to be 33.6% according to the final oxidation product, namely V_2O_5, which accounts for 52.5% of the total weight. The XPS spectrum of V 2p (Fig. S1c) was further collected, where the peaks at 516.7 and 524.2 eV manifest the existence of V^{4+}. [S6] The spectrum of S 2p showed in Fig. S1d can be deconvoluted into five components, among which a couple of peaks at 160.5 and 161.8 eV are assignable to the $2p_{3/2}$ and $2p_{1/2}$ of S^{2-}, another couple at 163.1 and 164.3 eV belong to C-S bond, and the remaining one at 168.3 eV derives from the sulfate species. [S7] The high resolution XPS spectrum of N 1s can be deconvoluted into three components (Fi g. S2e), namely graphitic N (401.1 eV), pyrrolic N (399.7 eV) and pyridinic N (399.2 eV), respectively. The C 1s spectrum also consist of three peaks (Fig. S2f), which are assignable to C-C (284.8 eV), C-S/C-N (286.2 eV) and C=O (288.3 eV) bonds, respectively. [S8]

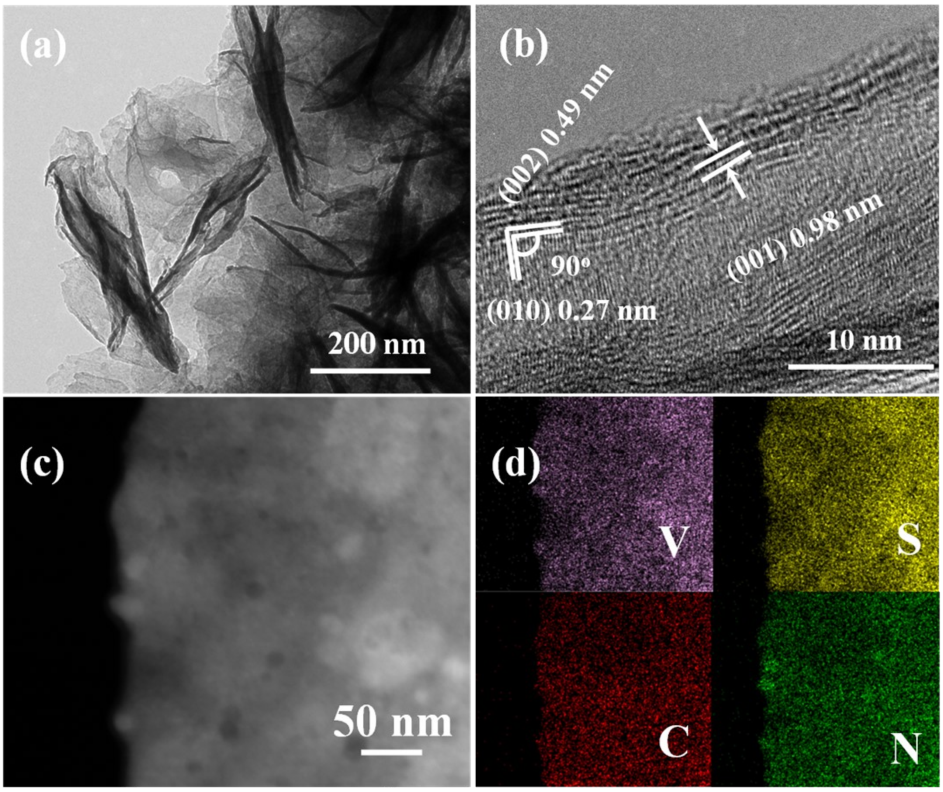

Fig. S2 (a) TEM image, (b) HR-TEM image, (c) HAADF-STEM image and corresponding (d) elemental mapping images of VS_2/SNC.

The transmission electron microscopy image (TEM) shown in Fig. S2a reflects that VS_2/SNC is assembled from nanosheets. As further observed from high-resolution TEM image (Fig. S2b), expanded (001), (002) and (010) crystal planes of VS_2 can be found. [S7] The mapping images of VS_2/SNC, as is shown in Fig. S2d, disclose the uniformly distributed elements of V, S, C and N.

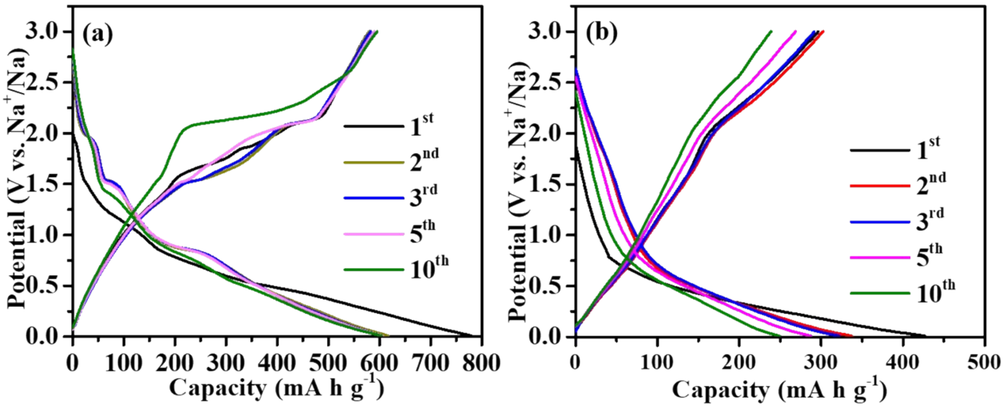

Fig. S3 Charge/discharge profiles of the VS_2/SNC electrodes with active material coated on the (a) Cu current collector and (b) Ti current collector, respectively. (Electrolyte: 1.0 M $NaPF_6$ DGM).

The charge/discharge profiles are completely different when the Cu (Fig. S3a) and Ti (Fig. S3b) current collectors were separately used. The redox platforms were almost unchanged when a Ti current collector was used, while they were constantly changing from the 1st to 10th cycles when a Cu current collector was used, which is consistent with that observed from the CV curves shown in Fig. 1b and 1c.

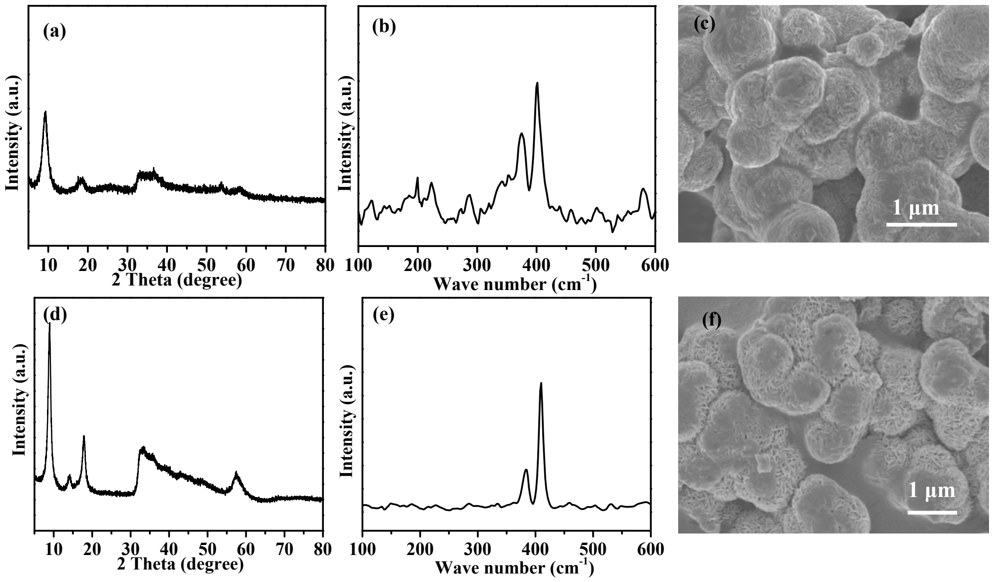

Fig. S4 (a, d) XRD patterns, (b, e) Raman spectra and (c, f) SEM images of (a, b, c) MoS_2 and (d, e, f) WS_2, respectively.

The XRD pattern of MoS_2 is displayed in Fig. S4a, in which the diffraction peak of (002) crystal plane is shifted to 2 θ = 9.2°, corresponding to an interlayer spacing of 0.96 nm. The peaks at 374.5 and 400.0 cm^{-1} in Raman spectrum (Fig. S4b) belong to the in-plane E_{2g}^{1} vibration and out-of-plane A_{1g} vibration of MoS_2. [S9] Similarly, the (002) crystal plane of WS_2 was also expanded to 0.98 nm with the diffraction peak moving to 2 θ = 8.9° (Fig. S4d). As displayed in Fig. S4e, the peaks for E_{2g}^{1} and A_{1g} vibrations of WS_2 are located at 385.5 and 409.9 cm^{-1}, respectively. [S10] As can be observed from Fig. S4c and 4f, both MoS_2 and WS_2 exhibit a morphology of aggregated micro-sphere assembled from nanosheets.

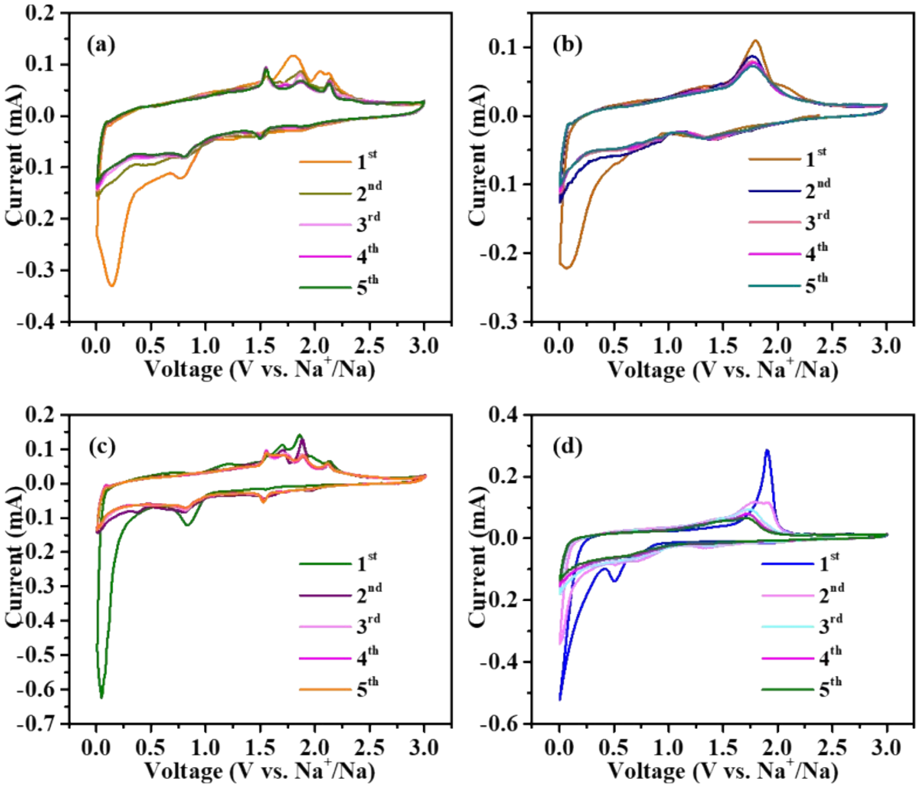

Fig. S5 CV curves for the electrodes of (a, b) MoS_2 and (c, d) WS_2 with the active materials coated on the (a, c) Cu and (b, d) Ti current collectors, respectively. (Electrolyte: 1.0 M $NaPF_6$ DGM).

As shown in Fig. S5a and S5c, regardless the active material is MoS_2 or WS_2, those redox peaks changed constantly as long as the Cu current collector was used. While in the case of using the Ti counterpart, the positions of those redox peaks remain almost constant (Fig. S5b and S5d). This phenomenon is consistent with that observed in VS_2/SNC electrode, indicating that Cu current collector participated in the electrochemical reactions of metal sulfides.

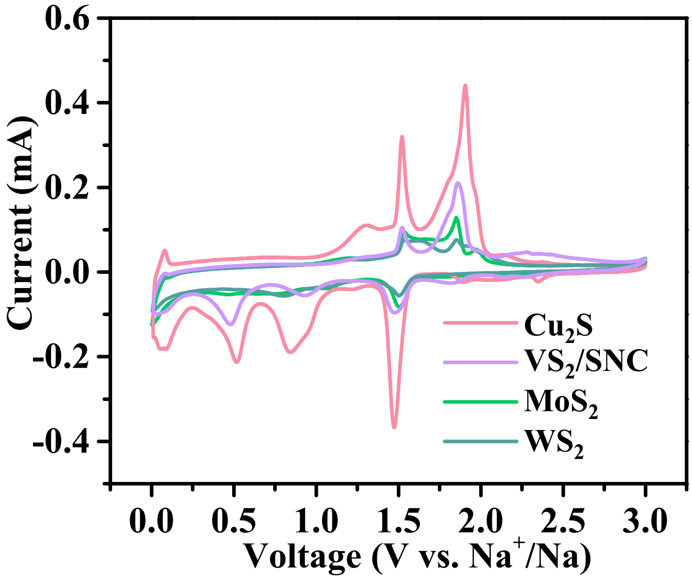

Fig. S6 CV curves for the electrodes of Cu_2S, VS_2/SNC, MoS_2 and WS_2 of the 52th cycles. (Electrolyte: 1.0 M $NaPF_6$ DGM; current collectors: Cu foils).

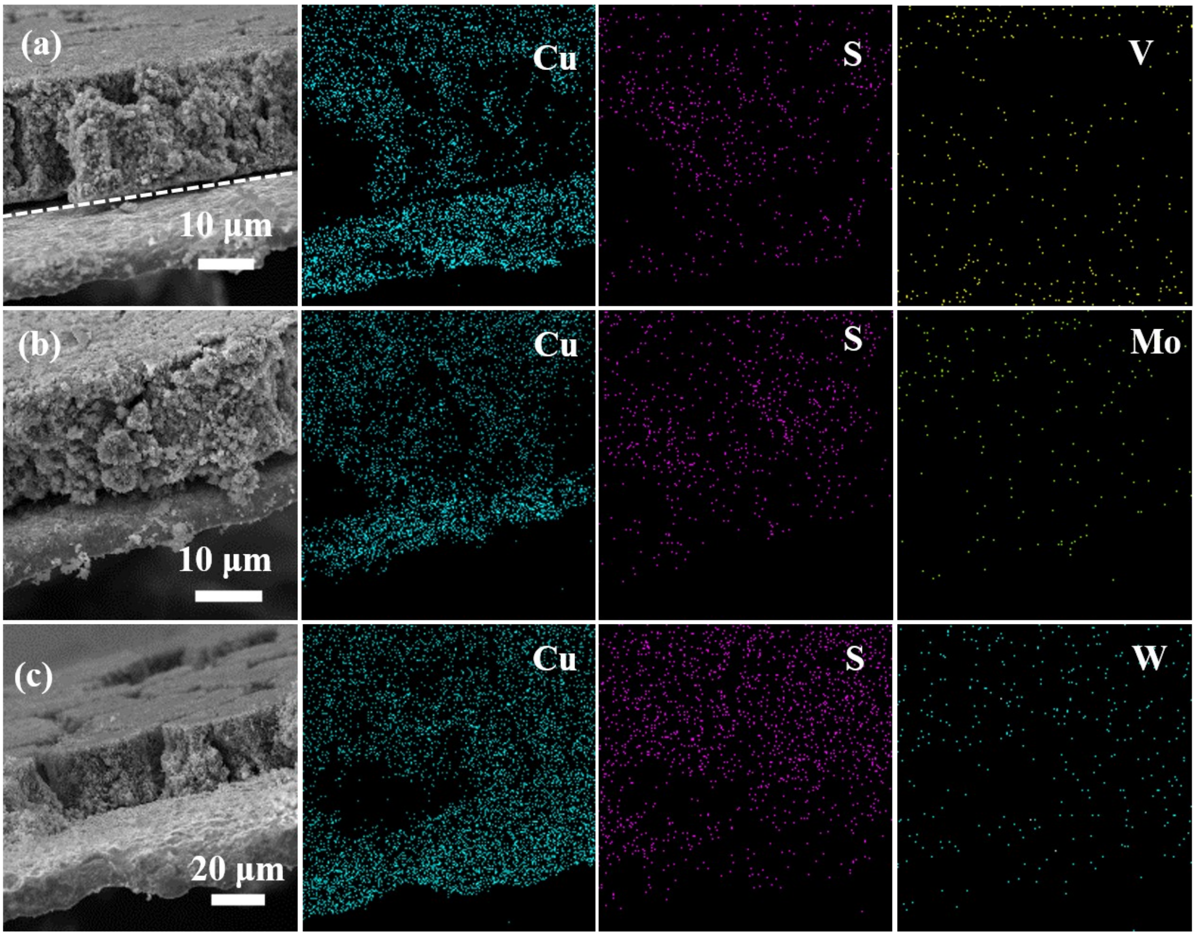

Fig. S7 Cross-section SEM images and corresponding element mapping images for the electrodes of (a) VS_2/SNC, (b) MoS_2, and (c) WS_2 which disassembled from the batteries cycled for 300 times, respectively.

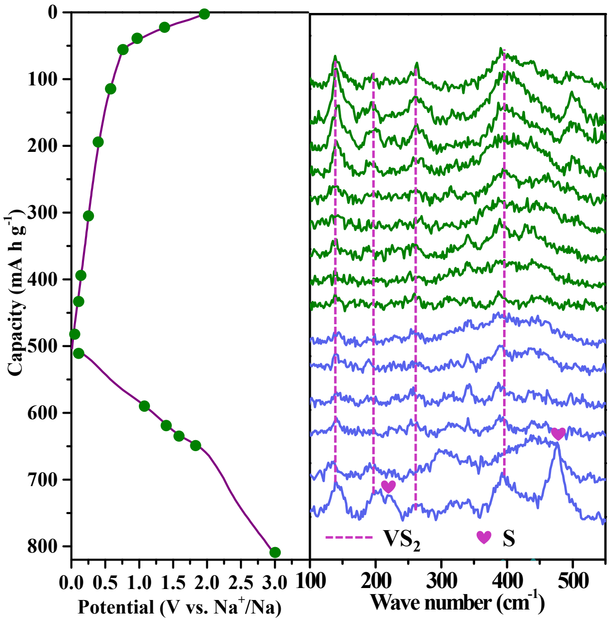

Fig. S8 In-situ Raman spectra of the VS_2/SNC electrode. (Current collector: Ti foil; electrolyte: 1.0 M $NaPF_6$ DGM).

As shown in Fig. S8, the four peaks at 143, 200, 265 and 399 cm^{-1} are assignable to the rocking and stretching vibrations of V-S bonds or their combination respectively, [S4] their intensities are almost unchanged as the battery was discharged from the initial state to 0.8 V, demonstrating the intercalation of Na^+ did not damage the original structure of VS_2. However, those peaks are greatly weakened at 0.6 V, and even vanish at 0.03 V, demonstrating that the V-S bonds were broken as the conversion reactions occurred. During the subsequent charge process, the signals of VS_2 become more and more conspicuous because of the recombination of V and Na_2S. When it was recharged to 1.7 V, another two peaks appeared at 221 and 476 cm^{-1} could be ascribed to sulfur, which results from the oxidization of Na_2S.

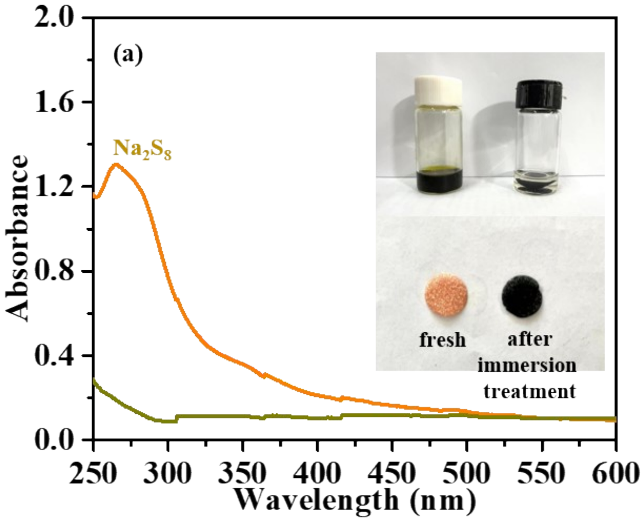

Fig. S9 UV-vis absorbance spectra of the Na_2S_8 DGM solutions with and without immersing Cu foam for 24 h, they were diluted 200 times with DGM before testing. The inset photographs compare the color changes of the solutions and Cu foams.

The Na_2S_8 solution was prepared by dissolving sulfur powder and Na_2S in DGM with a molar ratio of 7:1 inside an Ar-filled glove box. Then the solution was divided into two equal parts, one of which was added a piece of Cu foam with an area of 1.3 cm^2, the solution turned from dark yellow to transparent after standing for 24 h and the original Cu foam with metallic luster turned black. Those solutions were diluted 200 times with DGM before the UV-vis absorbance spectra were captured, as shown in Fig. S8, the strong absorption peak of Na_2S_8 is significantly weakened.[S11]

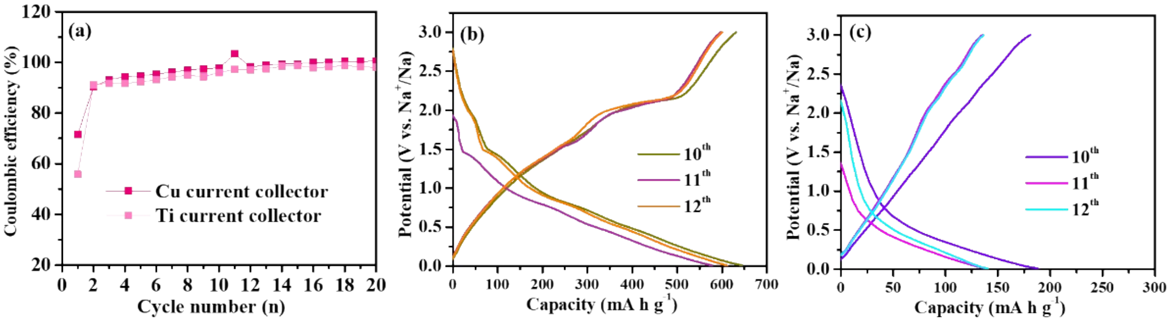

Fig. S10 Self-discharge tests of the VS_2/SNC electrodes when using the Ti and Cu current collectors respectively, the batteries were cycled for 10 times at 1.0 A g^{-1} and stood for 60 h after fully charged. (a) Coulombic efficiencies of the first 20 cycles. Charge/discharge profiles from the 10th to 12th cycle when using the (b) Cu or (c) Ti current collectors, respectively. (Electrolyte: 1.0 M $NaPF_6$ DGM).

After uninterrupted 10 cycles, the batteries were rested for 60 h, and then cycled further up to 20 cycles. As displayed in Fig. S10a, the Coulombic efficiencies (CE) of the 11th cycles are 105.1% and 97.2% when the Cu and Ti current collectors were separately used. On the first discharge after rest (11th), there is a drastic capacity decay when a Ti current collector was used with a capacity loss rate of 25.6%, while the application of a Cu current collector can effectively alleviate the shuttle effects, and the capacity loss rate is reduced to 5.4%. The above results suggest that the self-discharge of the batteries more likely stems from the irreversible loss of the active material in the case of using the Ti current collectors, while from the reversible polysulfide shuttle when using the Cu current collectors.[S12] The capacity loss rate is calculated based on equation S1:

$$\text{capacity loss rate (\%)} = \frac{C_{10th} - C_{11th}}{C_{10th}} \times 100\ \% \qquad \text{(S1)}$$

C_{10th}: the charge capacity of the 10th cycle

C_{11th}: the charge capacity of the 11th cycle

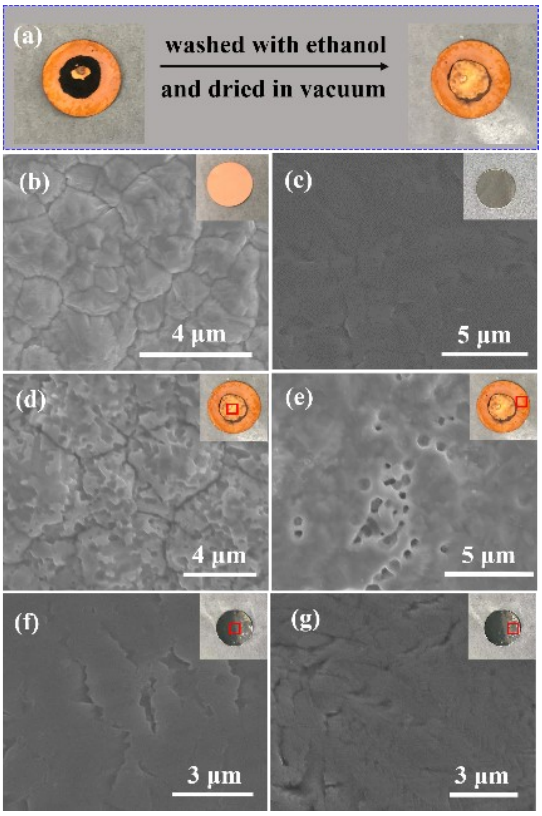

Fig. S11 (a) photographs of a partially coated VS_2/SNC electrode which disassembled from the battery cycled for 200 times. SEM images of the pristine (b) Cu and (c) Ti current collectors. SEM images of the (d, e) Cu and (f, g) Ti current collectors disassembled from the batteries cycled for 200 times, and the insets shows the areas from which the SEM images were captured. (Electrolyte: 1.0 M $NaPF_6$ DGM).

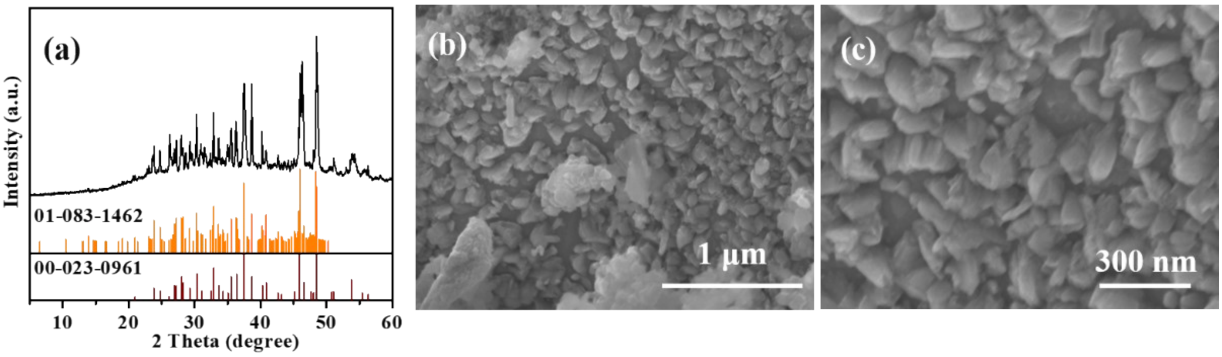

Fig. S12 (a) XRD pattern and (b, c) SEM images of the bulk Cu_2S.

In Fig. S12a, the bulk Cu_2S displays Bragg diffraction peaks corresponding to a mixture of orthorhombic phase Cu_2S (JCPDS NO. 00-023-0961) and the monoclinic phase Cu_2S (JCPDS NO. 01-083-1462). The SEM images displayed in Fig. S12b and S12c show the Cu_2S micron particles with irregularly shapes.

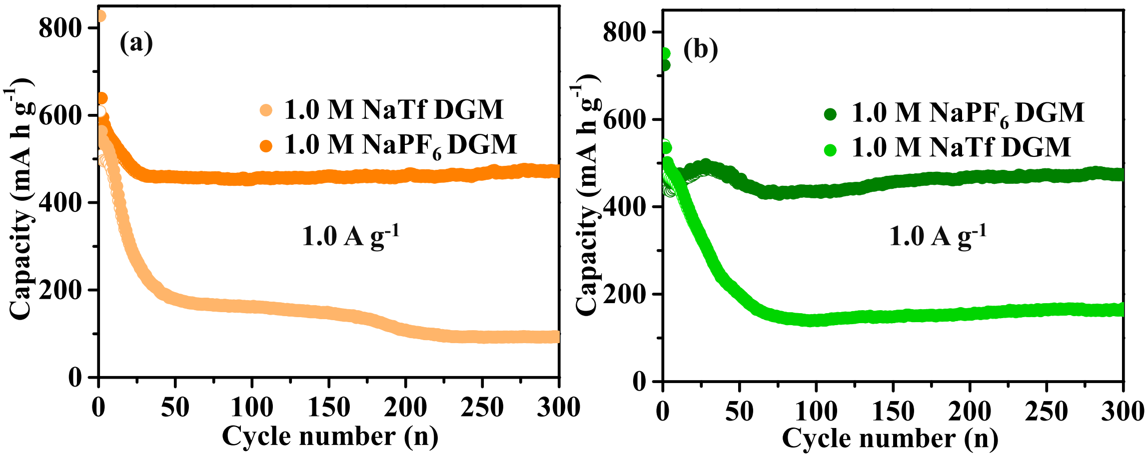

Fig. S13 Cycle performances of (a) MoS_2 and (b) WS_2 with active materials coated on Cu current collectors when different electrolytes were respectively used.

As demonstrated in Fig. S13, a favorable cycle stability is presented only when using the electrolyte of 1.0 M $NaPF_6$ DGM with a capacity retention of 471.3 mA h g^{-1} for MoS_2 (Fig. S13a) and 471.8 mA h g^{-1} for WS_2 (Fig. S13b) after 300 cycles, respectively. While in the case of using 1.0 M NaTf DGM, Cu current collector became ineffective in saving the drastic declined capacity of metal sulfides, specifically, the capacities for the electrodes of MoS_2 and WS_2 are both below 200 mA h g^{-1} after merely 50 cycles.

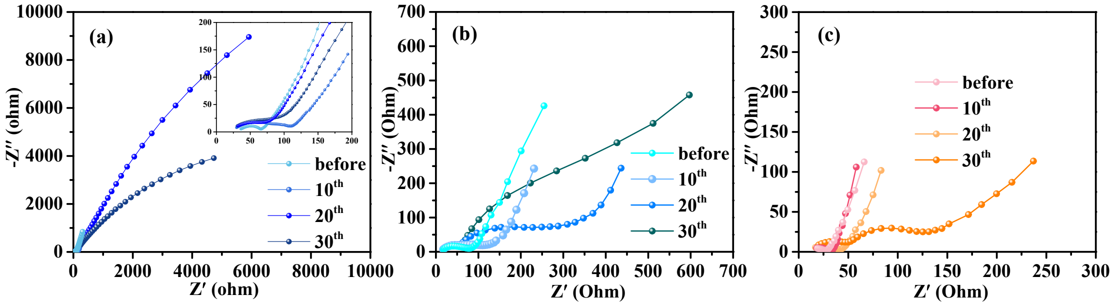

Fig. S14 Impedance analyses for the electrodes of (a) VS_2/SNC (b) MoS_2 and (c) WS_2 before cycling and cycling for 10, 20 and 30 times when using the electrolyte of 1.0 M NaTf DGM, respectively. (Current collectors: Cu foils).

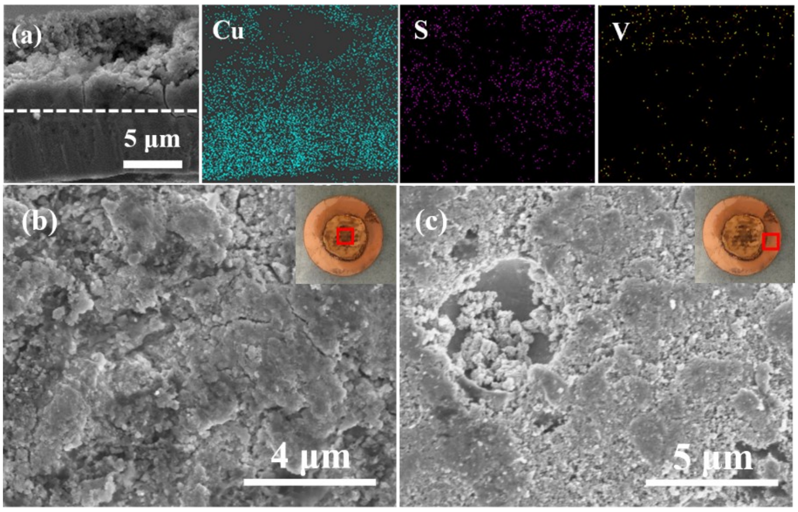

Fig. S15 (a) Cross-section SEM image and corresponding element mapping images of the VS_2/SNC electrode which disassembled from the battery cycled for 300 times. SEM images which captured from the areas of the Cu current collector that (b) coated and (c) uncoated with VS_2/SNC respectively. The insets show the photographs of the Cu current collector. (Electrolyte:1.0 M NaTf DGM).

As presented in Fig. S15a, the boundary of the Cu current collector and the active material become undistinguishable with a strong signal of Cu existing in the active material after 300 cycles, suggesting the Cu current collector also participated in the electrochemical reactions of the VS_2/SNC electrode when the electrolyte of 1.0 M NaTf DGM was used. The SEM images of the Cu current collector which was disassembled from the battery cycled for 200 times were also captured. The original morphology of the Cu current collector (Fig. S15b and S15c) has already been destroyed by the sulfur species, just like in the case of using 1.0 M $NaPF_6$ DGM.

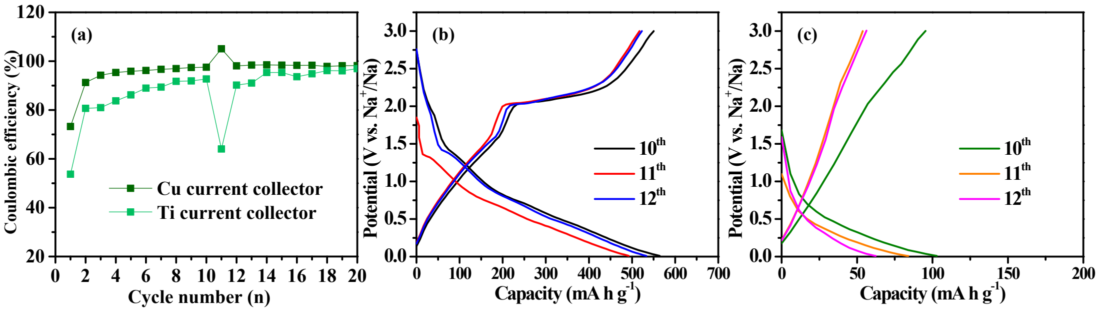

Fig. S16 Self-discharge tests of the VS_2/SNC electrodes when using the Ti and Cu current collectors respectively, the batteries were cycled for 10 times at 1.0 A g^{-1} and stood for 60 h after fully charged. (a) Coulombic efficiencies of the first 20 cycles. Charge/discharge profiles from the 10th to 12th cycle when using the (b) Cu or (c) Ti current collectors, respectively. (Electrolyte: 1.0 M NaTf DGM)

The CE of the 11th cycles are 103.3% and 67.0% when using the Cu and Ti current collectors, and the corresponding loss rates are 6.0% and 43.6% respectively, which reflects the Cu current collectors also possess the polysulfides immobilization capability in 1.0 M NaTf DGM.

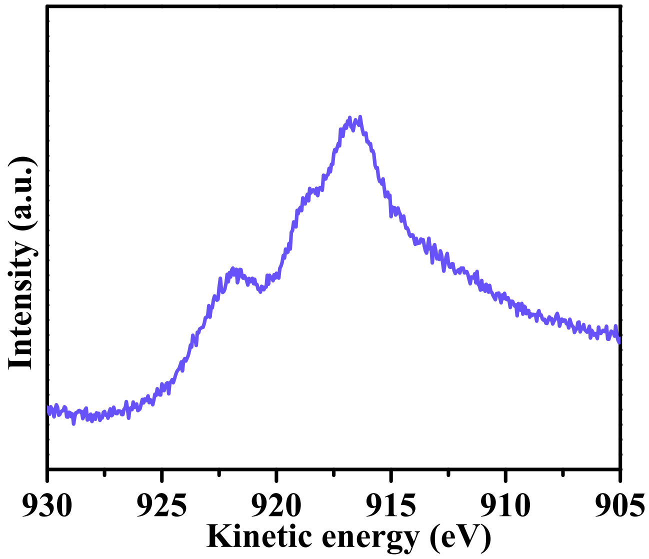

Fig. S17 Auger Cu LMM spectra of the VS_2/SNC electrode which was retrieved from the battery cycled for 200 times when using the electrolyte of 1.0 M NaTf DGM.

According to the Cu LMM spectrum presented in Fig. S17, the modified Auger parameter is calculated to be 1849.5 eV, indicating the dominant Cu (I) valence state. [S13]

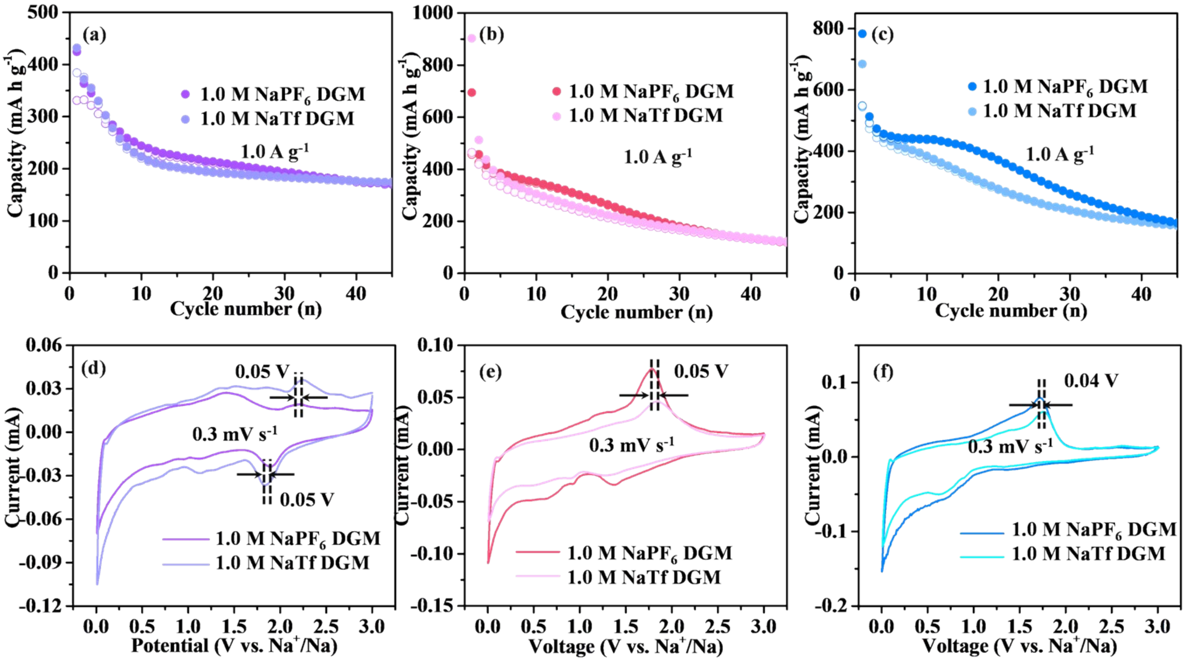

Fig. S18 (a-c) Cycle performances and (d-f) CV curves for the electrodes of (a, d) VS_2/SNC, (b, e) MoS_2 and (c, f) WS_2 when different electrolytes were respectively used. (Current collector: Ti foils)

As displayed in Fig. S18a, iInfluenced by the severe shuttle effects, a serious capacity decay is presented for the electrodes of VS_2/SNC when the Ti current collector was adopted no matter which electrolyte was used. Even so, a relative slower decay trend can be observed during the first 30 cycles when using the compatible one (1.0 M $NaPF_6$ DGM). A similar trend has also taken place for the electrodes of MoS_2 and WS_2 as displayed in Fig. S18b and 18c. Comparing the CV curves of the 4th cycle, an overpotential of 0.04 V for WS_2 (Fig. S18e) and 0.05 V for VS_2/SNC (Fig. S13d) and MoS_2 (Fig. S18f) can be observed.

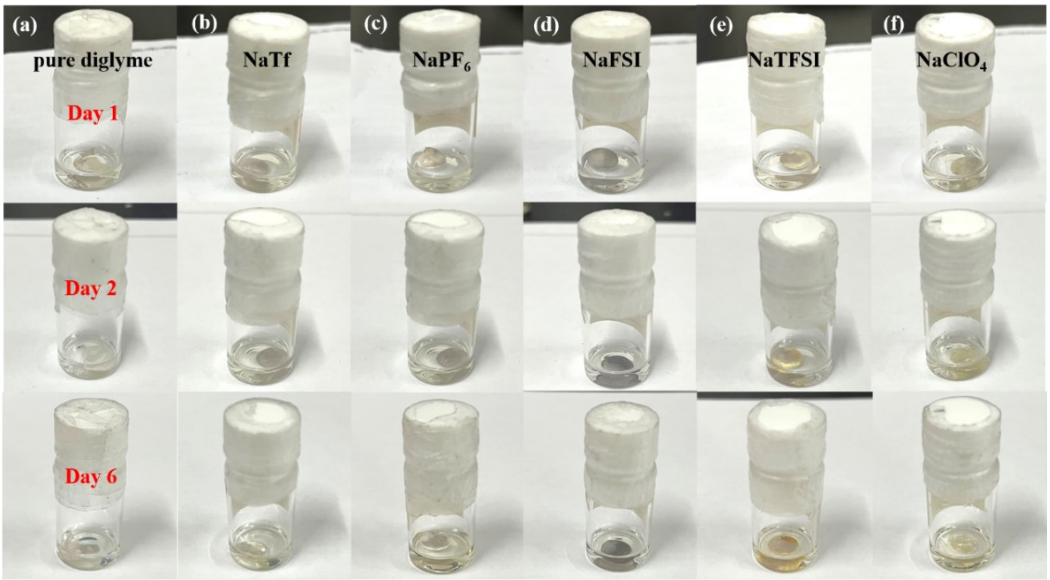

Fig. S19 Photo images of sodium metal exposed to (a) pure DGM (b) 1.0 M NaTf DGM, (c) 1.0 M $NaPF_6$ DGM, (d) 1.0 M NaFSI DGM, (e) 1.0 M NaTFSI DGM and (f) 1.0 M $NaClO_4$ DGM over several days, respectively. From top to bottom: Day 1, day2 and day 6.

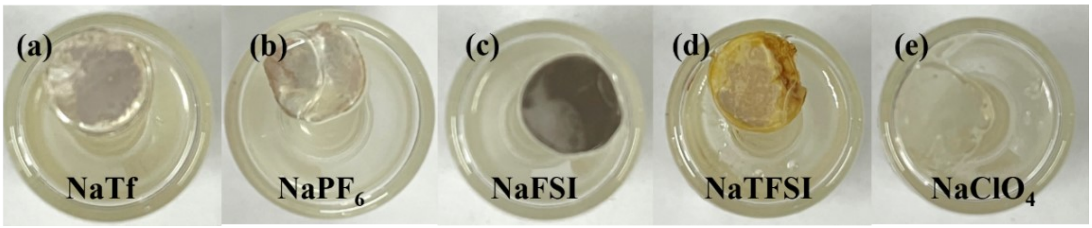

Fig. S20 Photo images of sodium metal exposed to (a) 1.0 M NaTf DGM, (b) 1.0 M $NaPF_6$ DGM, (c) 1.0 M NaFSI DGM, (d) 1.0 M NaTFSI DGM and (e) 1.0 M $NaClO_4$ DGM for 18 days.

The DN numbers for the anions of $TFSI^-$, ClO_4^- are 5.4 and 8.4 kcal mol^{-1} respectively, which are between that for the anions of PF_6^- (2.5 kcal mol^{-1}) and Tf^- (16.9 kcal mol^{-1}). [S14] Additionally, FSI^- also possesses a comparable DN value as that of $TFSI^-$. [S15] The stabilities of these salts to sodium electrode were first considered. As shown in Fig. S19, sodium metal was exposed to the different electrolyte solutions (and to pure diglyme as reference) for several days. For the salts of NaFSI and NaTFSI, rapid degradation of the sodium metal along with a color change took place. On the 18th day, the metallic nature of sodium was destroyed in most cases with NaTf and $NaPF_6$ being the exception (Fig. S20a and 20b). Severe corrosion has taken place in the presences of NaFSI and NaTFSI (Fig. S20c and 20d), and more seriously, the sodium metal was completely dissolved in the electrolyte of 1.0 M $NaClO_4$ DGM (Fig. S20e). Similar observations have been reported in other literature. [S16, S17]

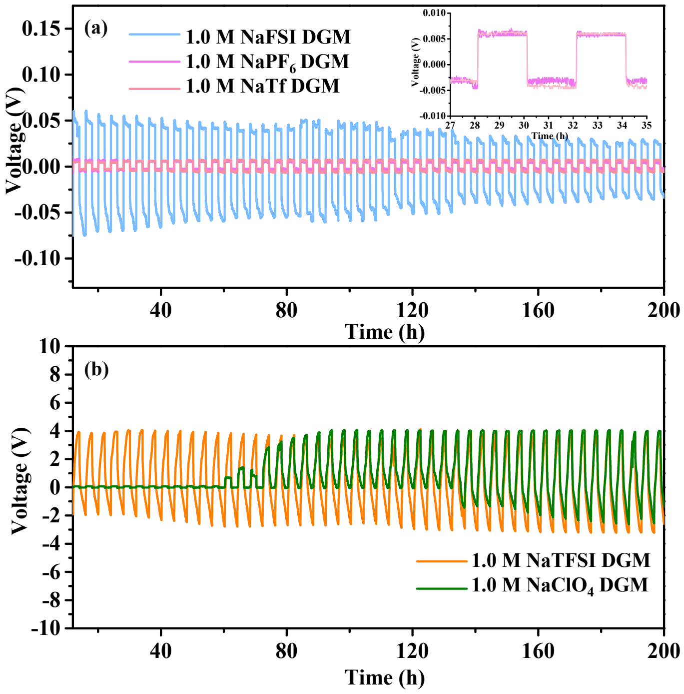

Fig. S21 Sodium plating/stripping measurements using Na|Na symmetric cells (9 µA cm^{-2}) when different electrolytes were used: in (a) 1.0 M NaFSI/NaPF$_6$/NaTf DGM and (b) 1.0 M NaTFSI/NaClO$_6$ DGM, respectively.

Symmetrical Na|Na cells were further assembled to evaluate the stability of the Na electrode in various electrolytes. The galvanostatic plating/stripping experiments were conducted at ±9 µA cm^{-2}, and each current pulse was applied for 120 min. As shown in Fig. S21, clear differences between the different salts can be seen. The largest overpotentials are found for NaTFSI and remains constant upon cycling, indicating a stable but, compared to the other salts, more resistive SEI. The smallest polarization is found for NaPF$_6$ and NaTf with about ±5 mV at ±9 µA cm^{-2}. The fluctuation in overpotential indicates an instable plating/stripping process in the presences of NaFSI. For NaClO$_4$, the situation is different. Starting with a relative low polarization, the plating/stripping overpotential increases during cycling, which is a clear sign for poor surface film formation and continuous electrolyte decomposition.

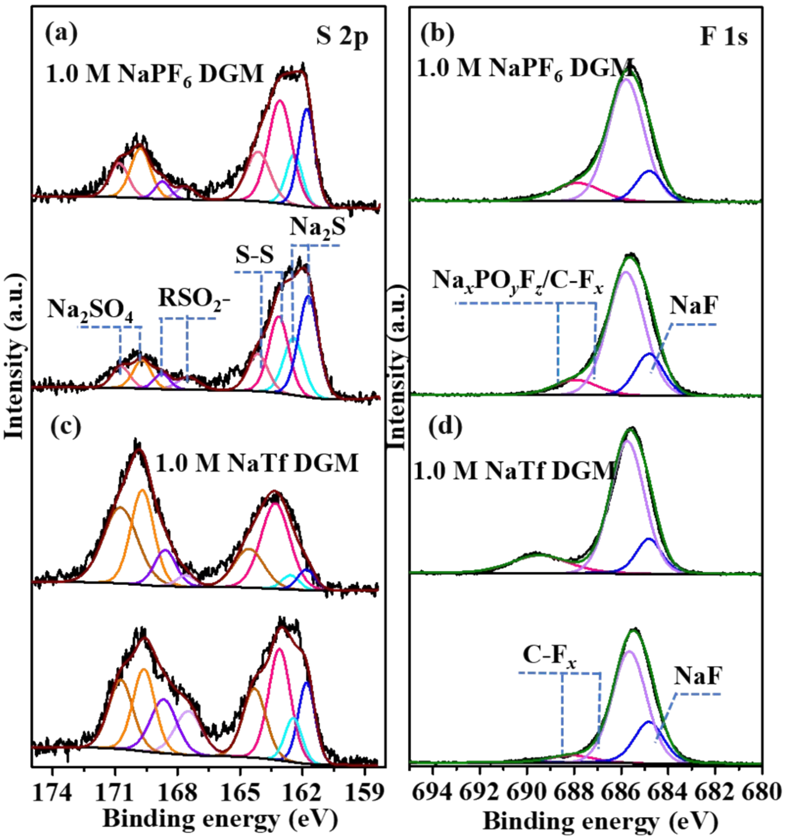

Fig. S22 High resolution XPS spectra of (a, c) S 2p and (b, d) F 1s for the electrodes of VS_2/SNC before (up) and after (bottom) 50 s of Ar-ion sputtering. The electrolytes of 1.0 M $NaPF_6$ DGM and 1.0 M NaTf DGM were respectively used.

In Fig. S22a, a couple of peaks at 169.6 and 170.7 eV belong to Na_2SO_4, and another couple at 167.5 and 168.7 eV are assignable to Na_2SO_3. [S18] Their peak intensities get stronger in the case of using the electrolyte of 1.0 M NaTf DGM because Na_2SO_4 and Na_2SO_3 are the decomposition products of NaTf, as Fig. S21c presented. In F 1s spectrum (Fig. 22b), the peak at 684.8 eV can be identified as NaF, of which the intensity gets stronger after sputtering, testifying its major existence in the interior of the SEI. Another two peaks at 685.6 and 689.6 eV derive from $NaPF_6$ decomposition product and polyvinylidene fluoride (PVDF) binder.[S19, S20] Since the anions of Tf^- and PF_6^- are both compatible with sodium electrode and present similar structure and component of SEI, further corroborating the difference in the electrochemical performances of metal sulfide comes from the donicity of PF_6^- and Tf^-.

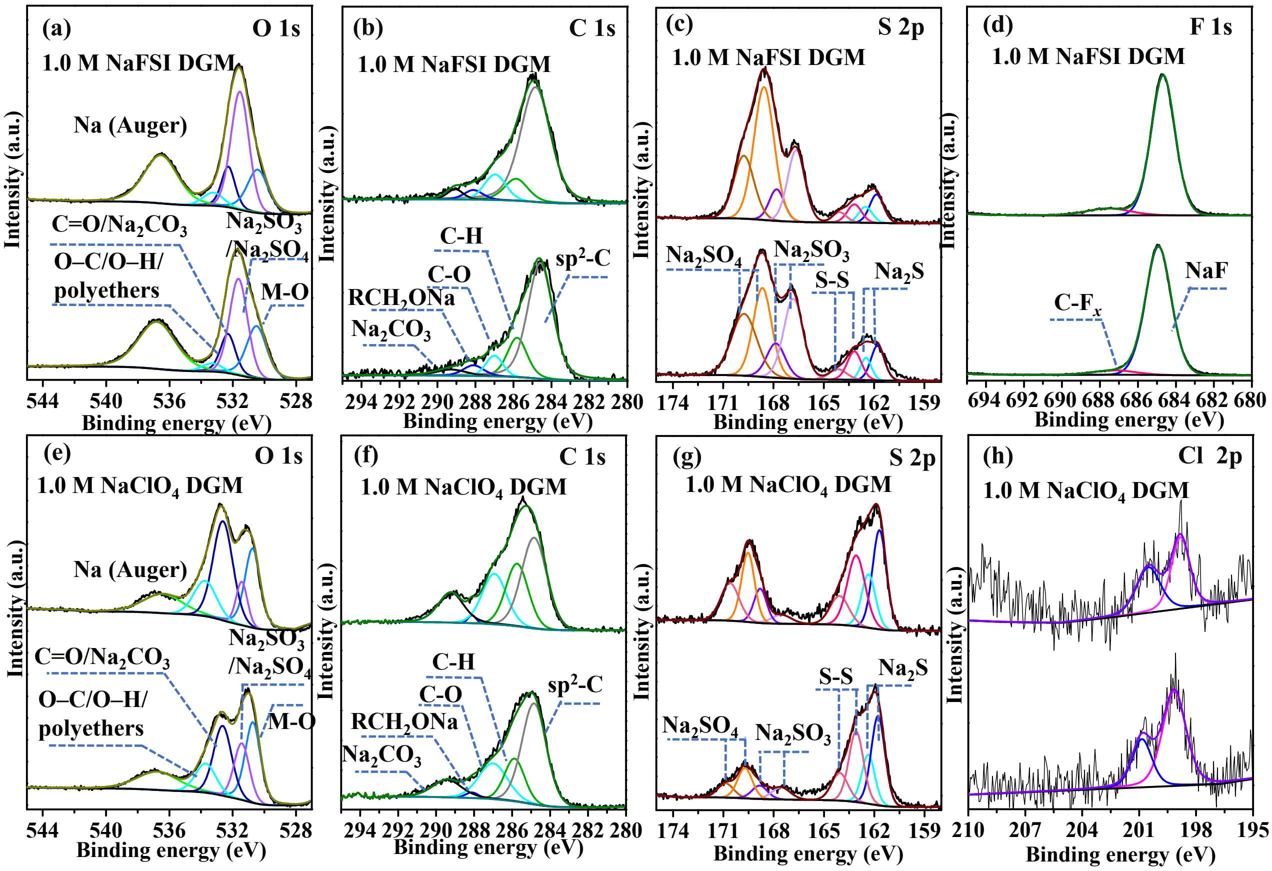

Fig. S23 XPS spectra of (a, e) O 1s, (b, f) C 1s, (c, g) S 2p (d) F1s and (h) Cl 2p collected from the cycled VS$_2$/SNC electrode before (top) and after (bottom) 50 s of Ar-ion sputtering. The electrolyte of 1.0 M NaFSI DGM and 1.0 M NaClO$_4$ DGM were respectively used.

The deconvoluted XPS spectra (Fig. S23a-23d) of the VS$_2$/SNC electrode cycled in the electrolyte of 1.0 M NaFSI DGM revealed that the SEI consists of similar components as those obtained in aforementioned cases, however, the main difference lies in their relative proportions and the overall quantity in oxygen-containing byproducts (Table 1). Specifically, the elements of Na, O and S account for a much higher atomic percent than in the aforementioned cases and little change has taken place even after 50 s of Ar-ion sputtering. Combined the the high-resolution XPS spectra of O 1s (Fig. S23a), S 2p (Fig. S23c) and F 1s (Fig. S23d), it can be speculated that large quantities of NaFSI decomposition byproducts, including NaF, Na$_2$SO$_3$ and Na$_2$SO$_4$, [S21] have been deposited on the VS$_2$/SNC electrode, which is dentrimental for Na$^+$ transport. When using the electrolyte of 1.0 M NaClO$_4$ DGM, the SEI interphase has different inorganic component, which doesn’t contain NaF but consits of NaCl and Na$_2$CO$_3$, and the latter species accounts for a large proporation and distributed in both the exterior and outerior of the SEI, as evidenced by the strong peaks at 532.6 eV in O 1s spectra (Fig. S23e) and 289.4 eV in C 1s spectra (Fig. S23f). Unfortunately, Na$_2$CO$_3$ is highly soluble in the electrolyte and its presence is fatal for the electrochemical performance. [S18, S22]

Table S1 The atomic percentages for the elements of C, O, F, Na, S and V in the SEI of VS_2/SNC electrodes when different electrolytes were respectively used. (The atomic percentages for the elements of C, O, F, Na, S and V are obtained from the XPS survey spectra)

Salt		NaTf		$NaPF_6$		NaFSI		$NaClO_4$	
Sputtering time		0 s	50 s	0 s	50 s	0 s	50 s	0 s	50 s
Element (atom%)	C	41.5	32.8	45.5	37.6	13.4	7.3	30.4	23.8
	O	11.9	9.2	10.6	8.6	22.0	18.8	21.6	18.5
	F (NaF)	2.7	5.1	2.3	3.7	16.5	20.1	–	–
	Na	20.3	29.7	19.6	27.4	31.0	38.9	14.8	19.4
	S	4.6	3.9	4.4	4.7	11.0	10.1	8.0	8.5
	V	3.6	3.7	2.9	2.6	2.4	2.4	4.3	4.9

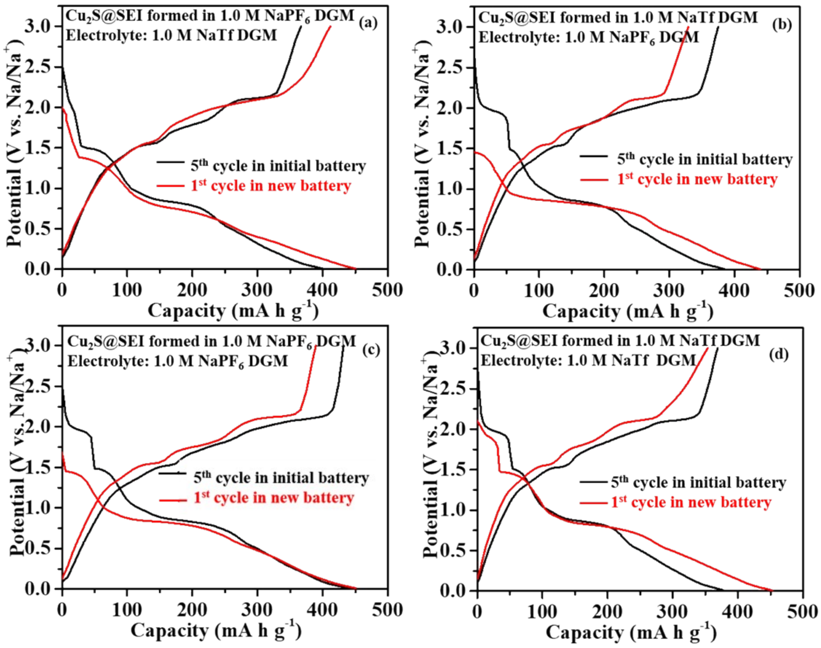

Fig. S24 The Cu_2S electrodes were cycled for 5 cycles first in the initial batteries when using (a, c) 1.0 M $NaPF_6$ DGM and (b, d) 1.0 M NaTf DGM respectively, and they were taken out from the batteries to obtain Cu_2S@SEI electrodes, then they were washed with DGM and dried directly after we taking it out from the initial batteries. Then, the dried Cu_2S@SEI electrodes were used for reassembling the new batteries. Charge/discharge profiles of the 5th cycle in the initial batteries and the 1st cycle in the new batteries after changing the electrolyte into (a) 1.0 M NaTf DGM, (b) 1.0 M $NaPF_6$ DGM, or changing (c, d) a fresh sodium electrode.

The charge/discharge profiles displayed in Fig. S24a and S24b correspond to the cycle performances shown in Fig. 3e, and that shown in Fig. S24c and S24d correspond to the cycle performances shown in Fig. 3f.

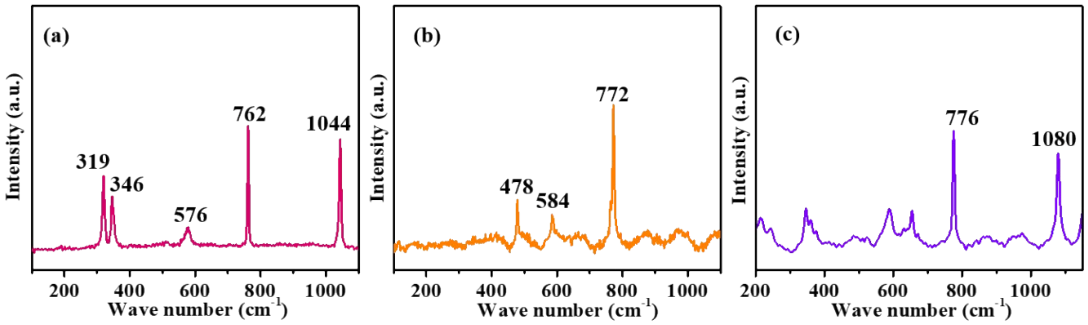

Fig. S25 Raman spectra of the (a) $NaCF_3SO_3$, (b) $NaPF_6$, and (c) $Cu(I)CF_3SO_3$ salts, respectively.

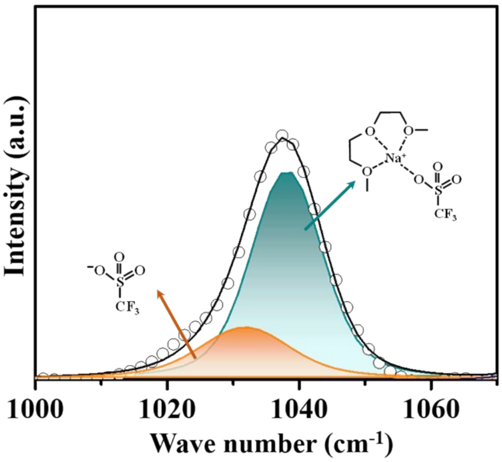

Fig. S26 Raman spectrum of the $v_s(SO_3)$ vibration in 1.0 M NaTf DGM. The spectrum was fitted with a Voigt function.

The peaks of stretching mode of SO_3 ($v_s(SO_3)$) can be deconvoluted into two components, namely free triflate anion (1032 cm^{-1}) and sodium-triflate monodentate ion pairs (1038 cm^{-1}) respectively, the area of the former only accounts for one thirds of the total area, demonstrating the electrolyte is dominated by the monodentate ion pairs due to the large ionic association strength of NaTf, which is consistent with the previously reported experiments and DFT calculation results. [S23]

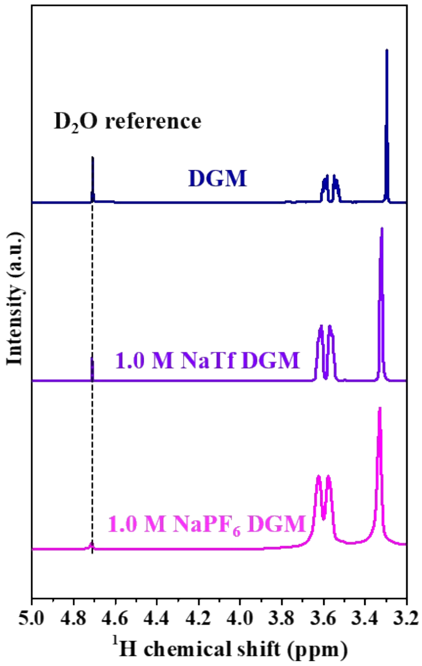

Fig. S27 ^{1}H-NMR spectra of DGM after adding NaTf salts and $NaPF_6$ salts respectively.

Fig. 4k is partial enlarged view of Fig. S27.

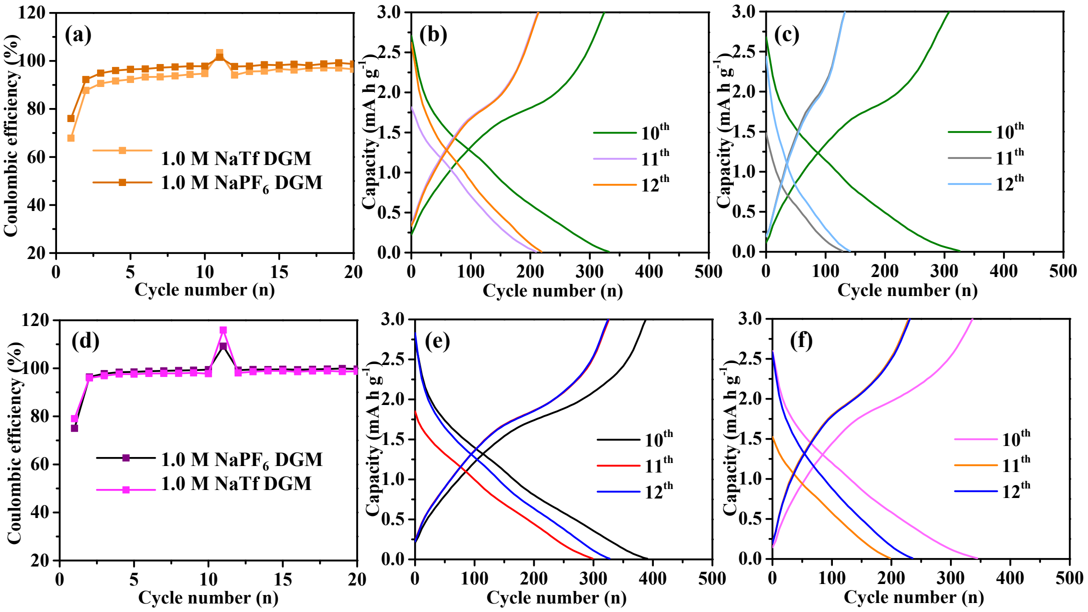

Fig. S28 Self-discharge tests for the electrodes of (a-c) MoS_2 and (d-f) WS_2 when different electrolytes were separately used, the batteries were cycled for 10 times at 1.0 A g^{-1} and stood for 60 h after fully charged. (a, d) Coulombic efficiencies of the first 20 cycles. Charge/discharge profiles from the 10th to 12th cycle when using the electrolytes of (b, e) 1.0 M $NaPF_6$ DGM and (c, f) 1.0 M NaTf DGM respectively. (Current collectors: Ti foils).

Table S2 The CE and capacity loss rate for the electrodes of VS_2/SNC, MoS_2 and WS_2 when different electrolytes were respectively used. (Current collectors: Ti foils)

electrolyte	1.0 $NaPF_6$ DGM			1.0 NaTf DGM		
electrode	VS_2/SNC	MoS_2	WS_2	VS_2/SNC	MoS_2	WS_2
CE (%)	97.2	101.5	109.2	67.0	103.4	115.9
Capacity loss rate (%)	25.5	34.4	16.0	43.6	56.9	31.8

Table S3 The calculated energy of $CF_3SO_3^-$, PF_6^-, and Na_2S_8 and their corresponding complexes using the B3LYP functional and def2-TZVP basis set.

Molecules	$CF_3SO_3^-$	PF_6^-	Na_2S_8
Energy/eV	-26173.56	-25606.48	-95527.95
Molecules		CF_3SO_3-Na_2S_8	PF_6-Na_2S_8
Energy/eV		-121703.05	-121135.49

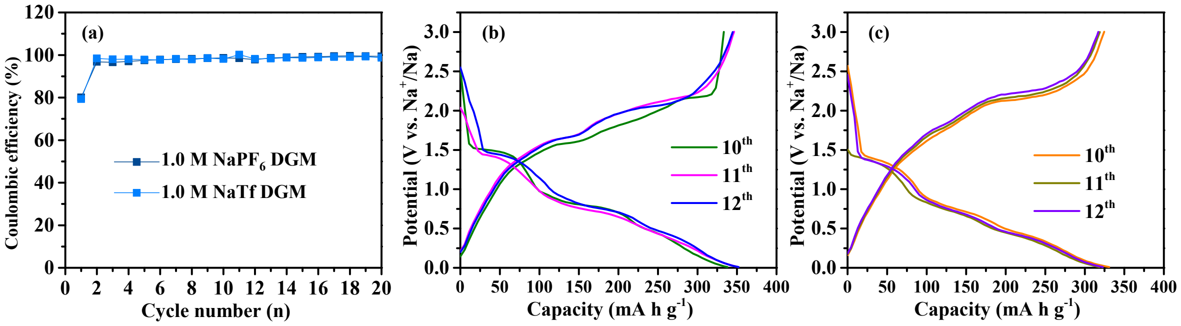

Fig. S29 Self-discharge tests of the Cu_2S electrodes when two types of electrolytes were separately used, the batteries were cycled for 10 times at 1.0 A g^{-1} and stood for 60 h after fully charged. (a) Coulombic efficiencies of the first 20 cycles. Charge/discharge profiles from the 10th to 12th cycle when using the electrolytes of (b) 1.0 M $NaPF_6$ DGM and (c) 1.0 M NaTf DGM respectively. (Current collectors: Ti foils).

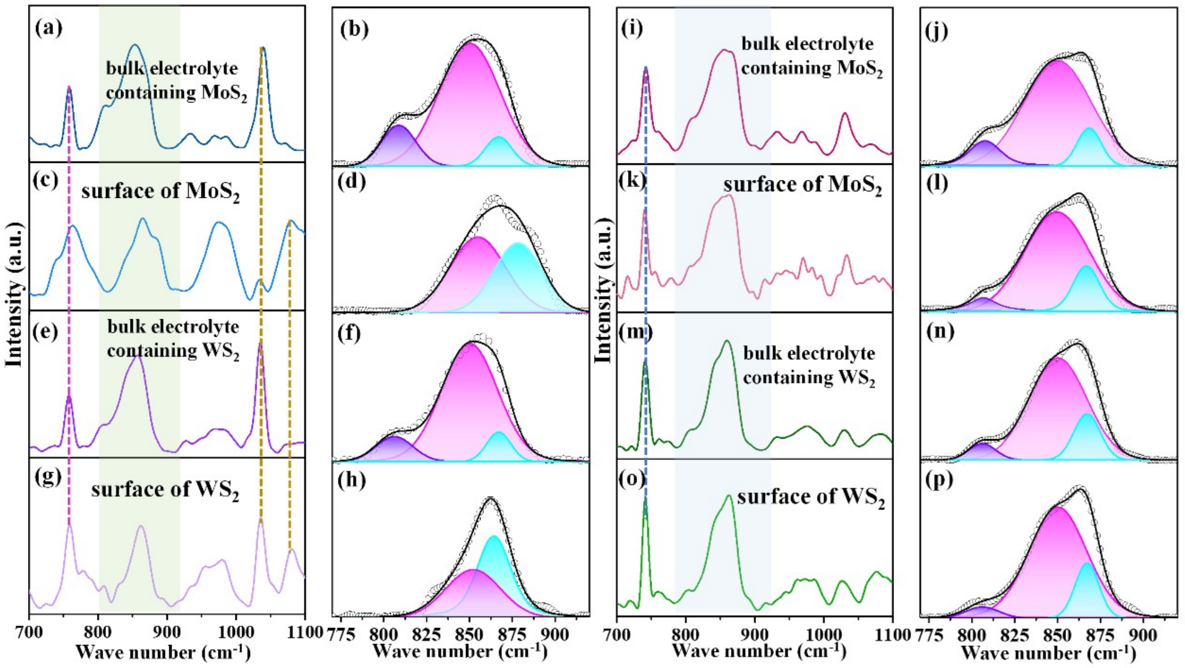

Fig. S30 Raman spectra of 1.0 M NaTf DGM which collected from the (a, e) bulk electrolytes, (c) surface of MoS_2 and (g) surface of WS_2. Raman spectra of 1.0 M $NaPF_6$ DGM which collected from the (i, m) bulk electrolytes, (k) surface of MoS_2 and (o) surface of WS_2. (b, d, f, h, j, l, n, p) The corresponding CH_2 rocking/C−O stretching vibrations of DGM which deconvoluted with a Voigt function.

Further investigating the interaction of anion and metal sulfides, equimolar quantities of MoS_2 and WS_2 were respectively soaked into the two types of electrolytes, subsequently, the Raman spectra were captured from the bulk electrolytes and the surfaces of metal sulfides. As is shown in Fig. 30a and 30e, the spectra acquired from the bulk electrolytes are basically unchanged in 1.0 M NaTf DGM, while significant changes have taken places in the spectrum that obtained from the surfaces of metal sulfides, specifically, the peak of $\delta_s(CF_3)$ exibit a positive shift for both MoS_2 and WS_2 (Fig. 30c and 30g). As for $v_s(SO_3)$, another new peak appeared at the higher wave number of 1079 cm^{-1} except the original one at 1038 cm^{-1}. Meanwhile, the solvated DGM molecules near the surface of the metal sulfides were greatly increased as demonstrated by the deconvoluted curves (Fig. 30d and 30h). As for the PF_6^- anion, it barely interacted with MoS_2 and WS_2 becaued those pectra (Fig. 30i-30p) are remained almost the same as that collected from the pure electrolyte.

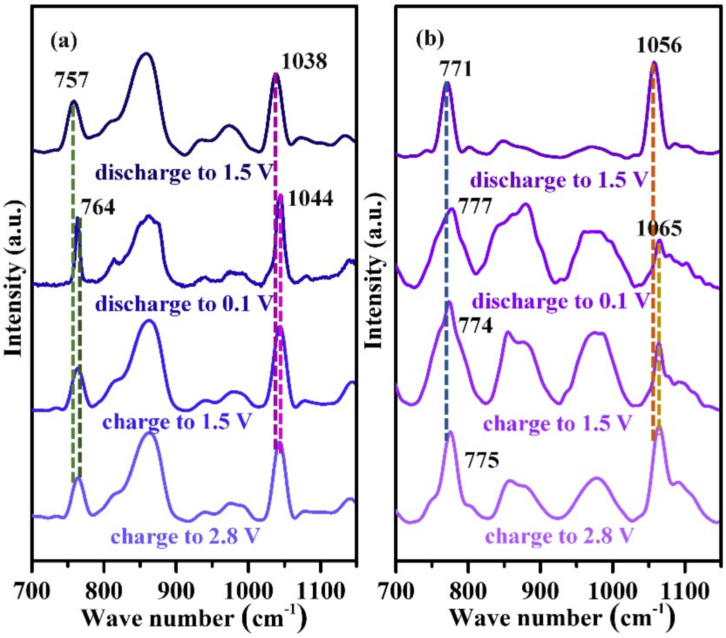

Fig. S31 Raman spectra collected from the surfaces of the (a) separators and (b) VS_2/SNC electrodes which disassembled from the batteries at different charge/discharge states of the 1st cycle. (Electrolyte: 1.0 M NaTf DGM; current collectors: Ti foils).

As shown in Fig. S31a, when the battery was discharged to 1.5 V, the peaks of $\delta_s(CF_3)$ and $v_s(SO_3)$ vibrations which collected from the separators shift to the higher wave numbers of 757 and 1038 cm^{-1} respectively. The blue shifts results from the interactions of triflate anions with soluble polysulfides, and more soluble polysulfides were produced with the conversion reactions progress on, therefore the interactions were intensified and the peaks shift to the higher wave numbers when the battery was discharged to 0.1 V, locating at 764 and 1044 cm^{-1} respectively. In addition, the corresponding spectra of the electrodes were also collected, as displayed in Fig. S31b, whatever the charge/discharge state, the peaks of $v_s(SO_3)$ and $\delta_s(CF_3)$ vibrations all exhibit larger positive shifts even if the SEI interphase has already formed compared with those collected from the separators, this results from two aspects: i) the interactions between triflate anions and polysulfides, ii) chelation of triflate anions with the central cations of VS_2/SNC.

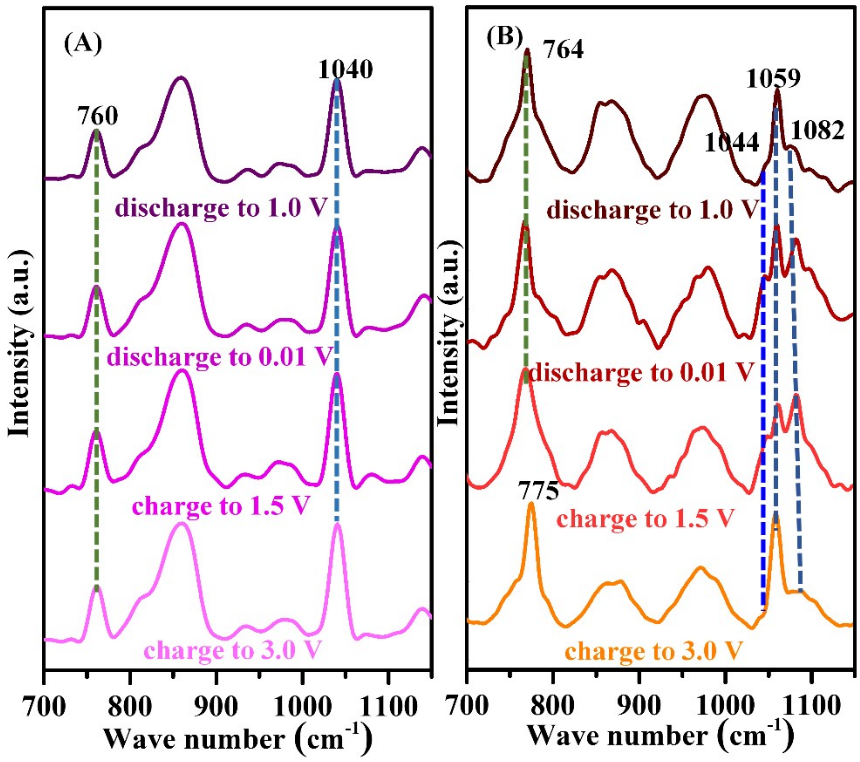

Fig. S32 Raman spectra collected from the surfaces of the (a) separators and (b) Cu_2S electrodes which disassembled from the batteries at different charge/discharge states of the 1st cycle. (Electrolyte: 1.0 M NaTf DGM; current collectors: Cu foils).

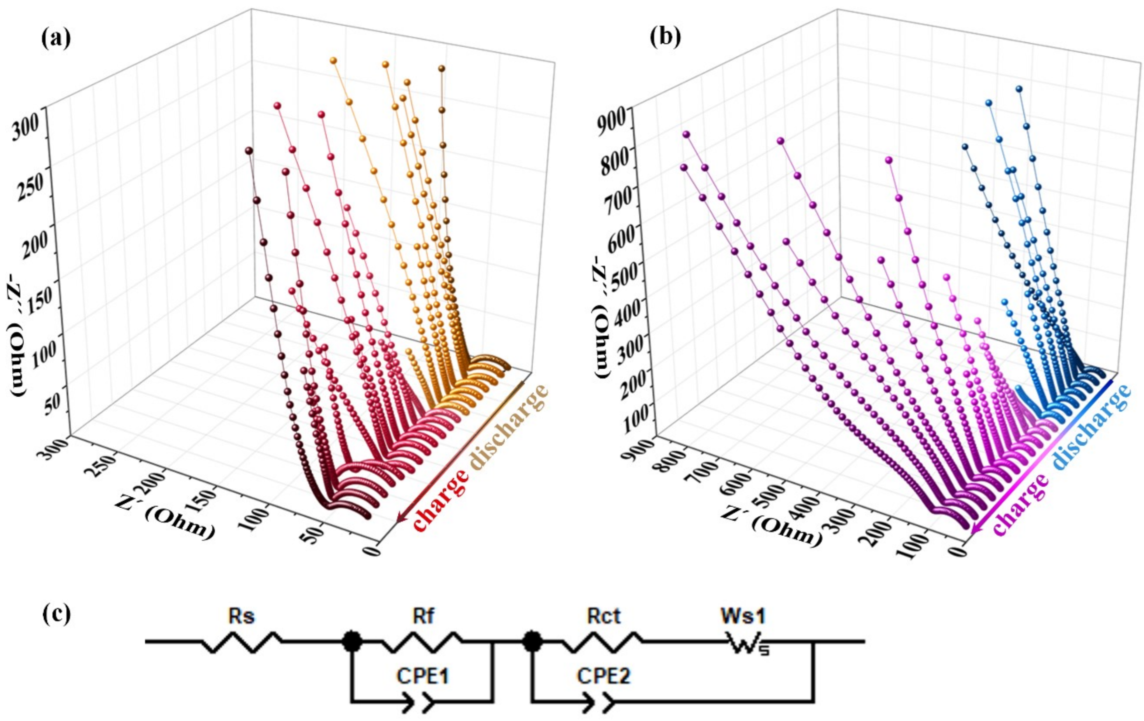

Fig. S33 In-situ EIS measurements of the Cu_2S electrodes for the 11th cycles when using (a) 1.0 M $NaPF_6$ DGM and (b) 1.0 M NaTf DGM, respectively. (c) The equivalent circuit used to fit the EIS spectra.

Table S4 The fitted parameters of the in-situ EIS spectra of Cu_2S electrode when 1.0 M $NaPF_6$ DGM and 1.0 M NaTf DGM were separately used.

Charge/discharge state	1.0 M $NaPF_6$ DGM			1.0 M NaTf DGM		
	R_s/Ω	R_f/Ω	R_{ct}/Ω	R_s/Ω	R_f/Ω	R_{ct}/Ω
discharge to 2.0 V	8.5	47.8	60.0	17.7	62.0	343.3
discharge to 1.8 V	9.3	42.4	32.0	17.4	65.5	65.0
discharge to 1.5 V	7.6	40.0	38.2	17.4	62.5	65.0
discharge to 1.2 V	10.1	40.0	38.2	17.3	63.3	65.0
discharge to 1.0 V	10.6	40.0	35.8	17.2	61.0	66.0
discharge to 0.5 V	10.0	39.0	37.7	17.5	69.3	66.8
discharge to 0.2 V	10.1	36.7	38.0	18.0	64.0	127.8
discharge to 0.01 V	11.3	37.6	38.0	18.0	59.5	133.4
charge to 0.3 V	10.0	40.8	40.0	18.6	60.4	58.8
charge to 0.6 V	10.0	41.8	38.7	17.4	64.0	68.0
charge to 0.9 V	11.2	41.0	39.0	17.8	66.7	68.4
charge to 1.2 V	10.1	40.7	40.0	17.5	66.0	72.0
charge to 1.4 V	9.0	40.0	38.3	17.3	70.3	70.0
charge to 1.7 V	10.0	34.8	37.6	17.9	80.4	80.9
charge to 2.0 V	11.1	53.8	43.8	18.6	76.1	85.0
charge to 2.3 V	10.3	40.6	46.4	17.4	80.0	290.0
charge to 2.6 V	11.0	51.7	49.1	18.0	84.7	432.0
charge to 2.8 V	11.0	47.7	42.0	18.7	88.7	440.0
charge to 3.0 V	9.7	47.2	38.1	19.8	85.1	413.8

R_s: ohmic resistance

R_f: resistance of the SEI

R_{ct}: charge transfer resistance

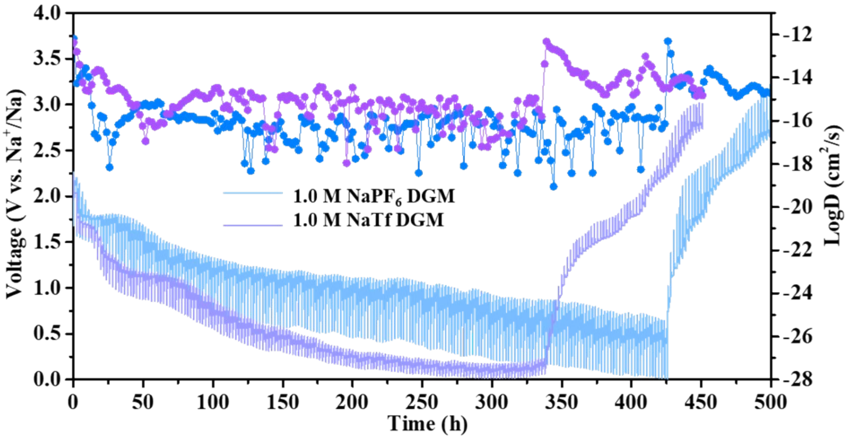

Fig. S34 GITT profiles of the Cu_2S electrodes and corresponding Na^+ diffusion coefficients at different potentials when using the electrolyte of 1.0 M NaTf DGM and 1.0 M $NaPF_6$ DGM, respectively.

Galvanostatic intermittent titration technique (GITT) was performed to investigate the apparent diffusion coefficients of Na^+. The batteries were charge/discharged at a current pulse of 0.1 A g^{-1} for a duration period of 8 min, followed by an open-circuit stand for 120 min to allow fully relaxation to a quasi-equilibrium potential. The diffusivity coefficients can be estimated according to Fick's second law as following equation (S2): [S25]

$$D = \frac{4}{\pi\tau}\left(\frac{m_B V_M}{M_B S}\right)^2\left(\frac{\Delta E_s}{\Delta E_t}\right)^2\left(\tau \ll \frac{L^2}{D}\right) \qquad \text{(S2)}$$

D is the diffusivity coefficient, τ is the pulse duration, M_B is molar mass of active mass, m_B and *S* are the active mass and surface area for the tested electrode, V_M is the molar volume, ΔE_s and ΔE_t can be obtained from the GITT profiles.

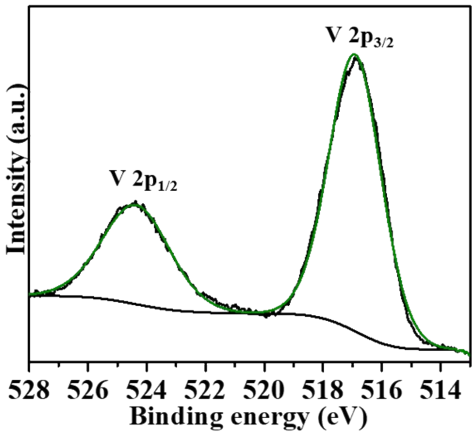

Fig. S35 XPS spectrum of V 2p which collected from the surfaces of VS_2/SNC after electrolyte soaking treatments in 1.0 M NaTf DGM.

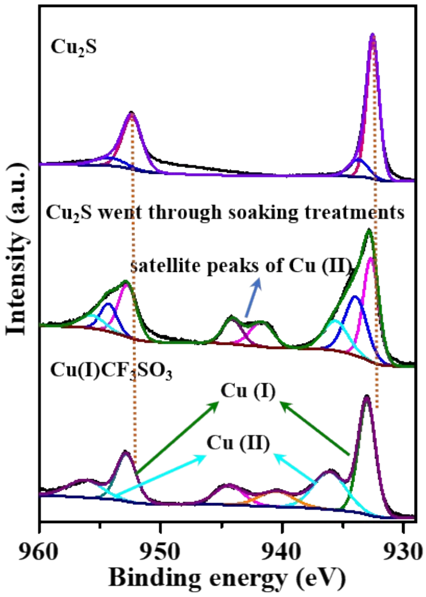

Fig. S36 XPS spectra of Cu 2p for Cu_2S, Cu_2S went through the electrolyte soaking treatment in 1.0 M NaTf DGM and Cu(I)CF_3SO_3 salts, respectively.

The Cu 2p spectrum of Cu_2S was significantly changed after going through the electrolyte soaking treatment in 1.0 M NaTf DGM, specifically, the original peaks of Cu (I) at 932.5 and 952.4 eV shift to the higher binding energies of 932.8 to 952.8 eV respectively, which get closer to the 933.0 and 953.0 eV of Cu(I)CF_3SO_3, testifying the interaction of Cu (I) and Tf^-. Besides, a new couple of peaks appeared at 935.7 and 955.7 eV, which results from the interaction of Cu (II) with Tf^-. The positive shifts of Cu (II) and Cu (I) result from the strongly electron-withdrawing inductive effects of Tf^-. The remaining peaks at 944.2 and 941.5 eV belong to the satellite peaks of Cu (II).

References

S1 M. J. Frisch, G. W. Trucks, H. B. Schlegel, G. E. Scuseria, M. A. Robb, J. R. Cheeseman, G. Scalmani, V. Barone, B. Mennucci, G. A. Petersson, H. Nakatsuji, M. Caricato, X. Li, H. P. Hratchian, A. F. Izmaylov, J. Bloino, G. Zheng, J. L. Sonnenberg, M. Hada, M. Ehara, K. Toyota, R. Fukuda, J. Hasegawa, M. Ishida, T. Nakajima, Y. Honda, O. Kitao, H. Nakai, T. Vreven, J. A. Montgomery, Jr., J. E. Peralta, F. Ogliaro, M. Bearpark, J. J. Heyd, E. Brothers, K. N. Kudin, V. N. Staroverov, T. Keith, R. Kobayashi, J. Normand, K. Raghavachari, A. Rendell, J. C. Burant, S. S. Iyengar, J. Tomasi, M. Cossi, N. Rega, J. M. Millam, M. Klene, J. E. Knox, J. B. Cross, V. Bakken, C. Adamo, J. Jaramillo, R. Gomperts, R. E. Stratmann, O. Yazyev, A. J. Austin, R. Cammi, C. Pomelli, J. W. Ochterski, R. L. Martin, K. Morokuma, V. G. Zakrzewski, G. A. Voth, P. Salvador, J. J. Dannenberg, S. Dapprich, A. D. Daniels, O. Farkas, J. B. Foresman, J. V. Ortiz, J. Cioslowski, and D. J. Fox, Gaussian, Inc., Wallingford CT, 2013.

S2 A. D. Becke, *J. Chem. Phys.* 1993, **98**, 5648-5652.

S3 F. Weigend, *Phys. Chem. Chem. Phys*., 2006, **8**, 1057-1065.

S4 P. He, M. Yan, G. Zhang, R. Sun, L. Chen, Q. An and L. Mai, *Adv. Energy Mater.,* 2017, **7**, 1601920.

S5 J. Xie, J. Zhang, S. Li, F. Grote, X. Zhang, H. Zhang, R. Wang, Y. Lei, B. Pan, and Xie, Yi, *J. Am. Chem. Soc.,* 2013, **135**, 17881-17888.

S6 X. Xue, R. Chen, C. Yan, P. Zhao, Y. Hu, W. Kong, H. Lin, L. Wang and Z. Jin, *Adv. Energy Mater.,* 2019, **9**, 1900145.

S7 W. Yang, N. Luo, C. Zheng, S. Huang and M. Wei, *Small* 2019, **15**, 1903904.

S8 C. Zheng, N. Luo, S. Huang, W. Wu, H. Huang and M. Wei, *ACS. Sustain. Chem. Eng.,* 2019, **7**, 10198-10206.

S9 P. Guo, K. Sun, D. Liu, P. Cheng, M. Lv, Q. Liu and D. He, *Electrochim. Acta.,* 2018, **283**, 646-654.

S10 X. Zhang, R. Zhao, Q. Wu, W. Li, C. Shen, L. Ni, H. Yan, G. Diao and M. Chen, *J. Mater. Chem. A,* 2018, **6**, 19004-19012.

S11 L. Tan, J. Yue, Z. Yang, X. Niu, Y. Yang, J. Zhang, R. Wang, L. Zeng, L. Guo and Y. Zhu, *ACS Nano* 2021, **15**, 11694-11703.

S12 L. Wang, J. Liu, S. Yuan, Y. Wang and Y. Xia, *Energy Environ. Sci.,* 2016, **9**, 224-231.

S13 D. Vaccarello, A. Tapley and Z. Ding, *RSC Adv*., 2013, **3**, 3512-3515,

S14 W. Linert, A. Camard, M. Armand and C. Michot, *Coordin. Chem. Rev.,* 2002, **226**, 137-141.

S15 P. Geysens, V. S. Rangasamy, S. Thayumanasundaram, K. Robeyns, L. V. Meervelt, J. P. Locquet, J. Fransaer and K. Binnemans, *J. Phys. Chem. B* 2018, **122**, 275-289.

S16 M. Goktas, C. Bolli, J. Buchheim, E. J. Berg, P. Novak, F. Bonilla, T. Rojo, S. Komaba, K. Kubota and P. Adelhelm, *ACS Appl Mater Interf.,* 2019, **11**, 32844-32855.

S17 L. Zhou, Z. Cao, J. Zhang, Q. Sun, Y. Wu, W. Wahyudi, J. Y. Hwang, L. Wang, L. Cavallo, Y. K. Sun, H. N. Alshareef and J. Ming, *Nano Lett.,* 2020, **20**, 3247-3254.

S18 M. Á. Muñoz - Márquez, M. Zarrabeitia, S. Passerini and T. Rojo, *Adv. Mater. Interf.,* 2022, **9**, 2101773.

S19 Z. Zhu, Y. Tang, Z. Lv,. J. Wei, Y. Zhang, R. Wang, W. Zhang, H. Xia, M. Ge and X. Chen, *Angew. Chem. Inter. Ed.,* 2018, **26**, 3658-3660.

S20 R. Mogensen, J. Maibach, W. R. Brant, D. Brandell and R. Younesi, *Electrochim. Acta.,* 2017, **245**, 696-704.

S21 E. Wang, Y. Niu, Y.-X. Yin and Y.-G. Guo, *ACS Mater. Lett.,* 2020, **3**, 18-41.

S22 P. Biswal, J. Rodrigues, A. Kludze, Y. Deng, Q. Zhao, J. Yin and L. A. Archer, *Cell Reports Physical Science* 2022, **3**, 100948.

S23 J. Wahlers, K. D. Fulfer, D. P. Harding, D. G. Kuroda, R. Kumar and R. Jorn, *J. Phys. Chem. C,* 2016, **120**, 17949-17959.

S24 K. Li, S. R. Galle Kankanamge and T. K. Weldeghiorghis, R. Jorn, D. G. Kuroda and R. Kumar, *J. Phys. Chem. C,* 2017, **122**, 4747-4756.

S25 W. Yang, L. Han, X. Liu, L. Hong and M. Wei, *J Colloid. Interf. Sci.,* 2020, **588**, 804-812.